remote sensing

MDPI

Article

Estimation of Infrared Stellar Flux Based on Star Catalogs with I-GWO for Stellar Calibration

Yang Hong [1,2,3], Peng Rao [1,2,*], Yuxing Zhou [1,2] and Xin Chen [1,2]

[1] Shanghai lnstitute of Technical Physics, Chinese Academy of Sciences, Shanghai 200083, China; hongyang@mail.sitp.ac.cn (Y.H.); zhouyuxing@mail.sitp.ac.cn (Y.Z.); chenxin@mail.sitp.ac.cn (X.C.)
[2] Key Laboratory of lntelligent lnfrared Perception, Chinese Academy of Sciences, Shanghai 200083, China
[3] University of Chinese Academy of Sciences, Beijing 100049, China
* Correspondence: peng_rao@mail.sitp.ac.cn

Abstract: As on-orbit space cameras evolve toward larger apertures, wider fields of view, and deeper cryogenic environments, achieving absolute radiometric calibration using an all-optical path blackbody reference source in orbit becomes increasingly challenging. Consequently, stars have emerged as a novel in-orbit standard source. However, due to differences in camera bands, directly obtaining the stellar radiance flux corresponding to specific camera bands is not feasible. In order to address this challenge, we propose a method for estimating radiance flux based on the MSX star catalog, which integrates a dual-band thermometry method with an improved grey wolf optimization (I-GWO) algorithm. In an experiment, we analyzed 351 stars with temperatures ranging from 4000 to 7000 K. The results indicate that our method achieved a temperature estimation accuracy of less than 10% for 83.5% of the stars, with an average estimation error of 5.82%. Compared with previous methods based on star catalogs, our approach significantly enhanced the estimation accuracy by 75.4%, improved algorithm stability by 91.3%, and reduced the computation time to only 3% of that required by other methods. Moreover, the on-orbit star calibration error using our stellar radiance flux estimation method remained within 5%. This study effectively leveraged the extensive data available in star catalogs, providing substantial support for the development of an infrared star calibration network, which holds significant value for the in-orbit calibration of large-aperture cameras. Future research will explore the potential applicability of this method across different spectral bands.

Keywords: stellar calibration; infrared star; star catalogs; grey wolf optimization

Citation: Hong, Y.; Rao, P.; Zhou, Y.; Chen, X. Estimation of Infrared Stellar Flux Based on Star Catalogs with I-GWO for Stellar Calibration. *Remote Sens.* **2024**, *16*, 2198. https://doi.org/10.3390/rs16122198

Academic Editors: Yonghua Jiang, Raad A. Saleh, Mingjun Deng and Litao Li

Received: 5 March 2024
Revised: 10 June 2024
Accepted: 15 June 2024
Published: 17 June 2024

1. Introduction

Infrared remote sensing imaging systems are strategically important in the military domain, such as in the space-based infrared system (SBIRS) and infrared search and tracking (IRST) [1]. Accurate infrared radiometric calibration technology provides the basis for accurate inversion of target radiation intensity, which is crucial for target classification and identification in military contexts. Although the sensor is radiometrically calibrated before a flight, the detector–response relationship changes after orbit due to environmental changes, time drift, and so on [2]. Therefore, high-precision radiometric calibration in orbit is essential. At present, most on-orbit infrared reference sources are blackbodies, which can realize high-precision absolute and relative radiometric calibration. However, as on-orbit space cameras evolve toward larger apertures, wider fields of view, and deeper cryogenic technologies, the practicality of blackbodies is constrained by the limited resources in orbit. This is particularly true for calibration of the full optical path and low-end detector responses. Consequently, scholars have suggested employing stars as an all-optical absolute radiometric calibration reference source. Stars offer advantages such as low radiation values, long-term stability, and traceability [3]. The midcourse space experiment (MSX) currently uses an internal blackbody combined with five standard stars (αLyr, αCma, αTau, βGem, and αBoo) and reference spheres as the on-orbit reference source, with a calibration

accuracy of roughly 2–5% [4–6]. Similarly, the infrared array camera (IRAC) is an infrared camera system on the Spitzer Space Telescope which uses bright A-type stars as a reference source for calibrations, with a calibration accuracy of 3% [7]. The James Webb Space Telescope (JWST) leverages five spectroscopically modeled stars (including white dwarfs and A and G stars) at the 1% level with a design calibration accuracy of about 5% [8]. However, due to the differences in observational wavelengths used in non-astronomical fields, such as remote sensing and space-based target detection, compared with those used in astronomy, there remains uncertainty in understanding the true flux density of stars. Therefore, acquiring high-precision stellar flux data in nonstandard wavelengths is crucial for the on-orbit calibration of space cameras.

Stellar radiative fluxes are mainly affected by stellar spectral model parameters, such as the effective temperature, emissivity, and angular diameter, and can therefore be estimated from the stellar spectral parameters [9–11]. Kurucz proposed a stellar spectral model that fits the stellar spectral distribution using parameters such as the temperature, surface gravity field, and metal abundance, with fitting errors in the range of 3–5% [12]. For improved radiation flux accuracy, Rieke used interpolation for A-type and solar-type stars in combination with the Kurucz model to obtain special information in the range of 1–25 μm, with an accuracy of approximately 2% [13,14]. Rebassa-Mansergas et al. used the Sloan Digital Sky Survey (SDSS) with spectral template fitting to estimate the spectral parameters, such as the stellar temperature and surface gravity [15]. Nonetheless, such methods require a large amount of observational data, or they will limit the number of calibrated stars by targeting only certain types of stars.

Recently, it has been proposed to leverage the vast amount of stellar information in catalogs for flux estimation [16,17]. This type of method focuses on estimating stellar spectral parameters from catalog information to construct stellar spectra. Zhang et al. used the stochastic particle swarm optimization (SPSO) method to estimate the stellar temperature and the observation angle [17]. However, due to the different compositions of stellar atmospheres, stellar spectra have different emissivity values at different wavelengths, resulting in spectra that are not identical to a blackbody, which can lead to certain estimation errors [18,19]. Therefore, Zhang used stochastic particle swarm optimization to estimate the stellar emissivity for stellar radiation flux estimation, and the accuracy of this method, based on the MSX catalog, was approximately 5% [20]. Despite this, the extrapolation accuracy of such methods still cannot meet the required accuracy of our on-orbit space camera calibrations. In response, we further carried out a study on the estimation of stellar infrared radiation fluxes based on stellar catalog information. Harnessing a wealth of observations from existing catalogs, we expanded the infrared standard stellar network, enabling the targeted selection of extensive stellar data for precise on-orbit radiometric calibrations.

The observation of stars in orbit is constrained by the detector's field of view, which only allows for the monitoring of celestial bodies within specific regions. The scarcity of calibration stars fails to satisfy the demand for frequent calibrations, necessitating the development of a method that can obtain a large number of calibration stars to support rapid correction cycles and real-time performance evaluation. Incorporating more calibration stars helps to mitigate the randomness associated with observations that depend on a limited number of stars. The star catalogs encompass diverse star types and luminosities. Fully utilizing the information in catalogs for extrapolation can provide more possibilities for the selection of calibration stars. Consequently, this study primarily investigates methods for estimating stellar radiance flux, which are notably more efficient and cost-effective. It leverages the rich data available in star catalogs to advance the calibration of instruments in spaceborne platforms.

In order to further enhance the accuracy of estimating stellar radiation flux based on the catalogs, we introduce a novel method that integrates a dual-band thermometry approach with an improved grey wolf optimization (I-GWO) algorithm. The challenge of estimating stellar spectral parameters from catalog information lies in the disparity between the number of unknowns and the available equations, primarily due to emissivity

variability across different wavelengths. This discrepancy often leads to reduced estimation accuracy and instability. In order to mitigate this issue, we consider starting by reducing the unknown quantities through the use of the catalog information to estimate the effective stellar temperature using the dual-band thermometry method. The subsequent estimation of the remaining spectral parameters is then performed using additional band information. The choice of the optimization algorithm is also important in influencing the accuracy of the parameter estimation. Thus, we used the I-GWO algorithm to estimate the specific spectral band emissivity as well as the stellar observation angles. Furthermore, to enhance computational efficiency, we introduced isophotal radiative flux reduction, which simplifies the computational complexity. Consequently, the proposed method can effectively and efficiently estimate the radiative flux of stars in specific spectral bands, providing support for in-orbit radiometric calibration.

Our contributions can be summarized in four main areas. (1) We introduce a dual-band thermometry method to accurately estimate stellar temperatures, providing a solid foundation for any subsequent estimations of stellar radiative flux. (2) Utilizing a stellar spectral model that incorporates emissivity, we propose using the I-GWO algorithm to estimate spectral parameters such as the band emissivity and star observation solid angle. (3) Substitution of full spectral band integration with isophotal radiative flux is carried out to enhance computational efficiency. (4) We estimate the radiative flux of stars at specific camera wavelengths and validate the accuracy of this method through in-orbit experiments, supporting its applicability to in-orbit calibration.

2. Materials and Methods

In this study, the proposed method addresses the problem of estimating stellar flux from two perspectives. Initially, it utilizes the dual-band thermometry method to estimate the stellar temperature, which effectively reduces the number of unknown parameters, thereby enhancing the stability and accuracy of emissivity and observation angle estimations. Secondly, the I-GWO algorithm is used to find the optimal emissivity and observation angle values. Moreover, our approach introduces isophotometric radiation flux instead of whole-wavelength integration to improve computational efficiency. The flow of our proposed method is shown in Figure 1.

2.1. Stellar Observation Model

Stellar spectral radiation models are frequently approximated using blackbody radiation principles. However, this simplification does not account for the complex realities of stellar atmospheres, where gases of varying pressures, densities, and chemical compositions can introduce significant absorption or emission spectral lines in certain bands, diverging from blackbody predictions [20]. In stellar spectra, two primary components are typically observed: the continuum spectrum and the absorption lines or bands. The continuum spectrum originates in the outermost layer of the stellar atmosphere, the photosphere, while the absorption lines and bands are formed by the absorption of photons by atoms and molecules in the stellar atmosphere [21]. Consequently, stellar spectral emission models exhibit discrepancies with blackbody radiation, particularly in terms of band emissivity, underscoring the need for more nuanced modeling approaches.

The observed stellar radiative flux is not only determined by the star's temperature but also significantly influenced by the observational solid angle subtended by the star. In order to streamline the analysis and simplify the observational model, three primary parameters are typically considered: the star's temperature, the observing angle, and the emissivity of the stellar surface. Utilizing the blackbody radiation model and Planck's law, a detector-based stellar observation model can be constructed:

$$E_\lambda(\varepsilon_\lambda, \Omega, T) = \varepsilon(\lambda) \times \Omega \times \frac{c_1 \lambda^{-5}}{\exp\left(\frac{c_2}{\lambda T}\right) - 1} \quad (1)$$

where $E_\lambda(\varepsilon_\lambda, \Omega, T)$ is the stellar radiation flux at a wavelength of λ, ε_λ is the emissivity at λ, Ω is the stellar observation solid angle, T is the stellar temperature, and c_1 and c_2 are the radiation constants. The star observation solid angle is $\Omega = \frac{\pi r^2}{R^2}$, where r represents the radius of the star, and R signifies the distance from the star to the observation point. Given the vast distances between stars and Earth, observed stars are typically treated as point-like objects. Additionally, the relative distance between the detectors used for compiling star catalogs and our detectors is negligible compared with their distance to the stars. This means that the star observation solid angle is consistent, thereby allowing us to use the information in star catalogs to estimate the star observation solid angles of stars.

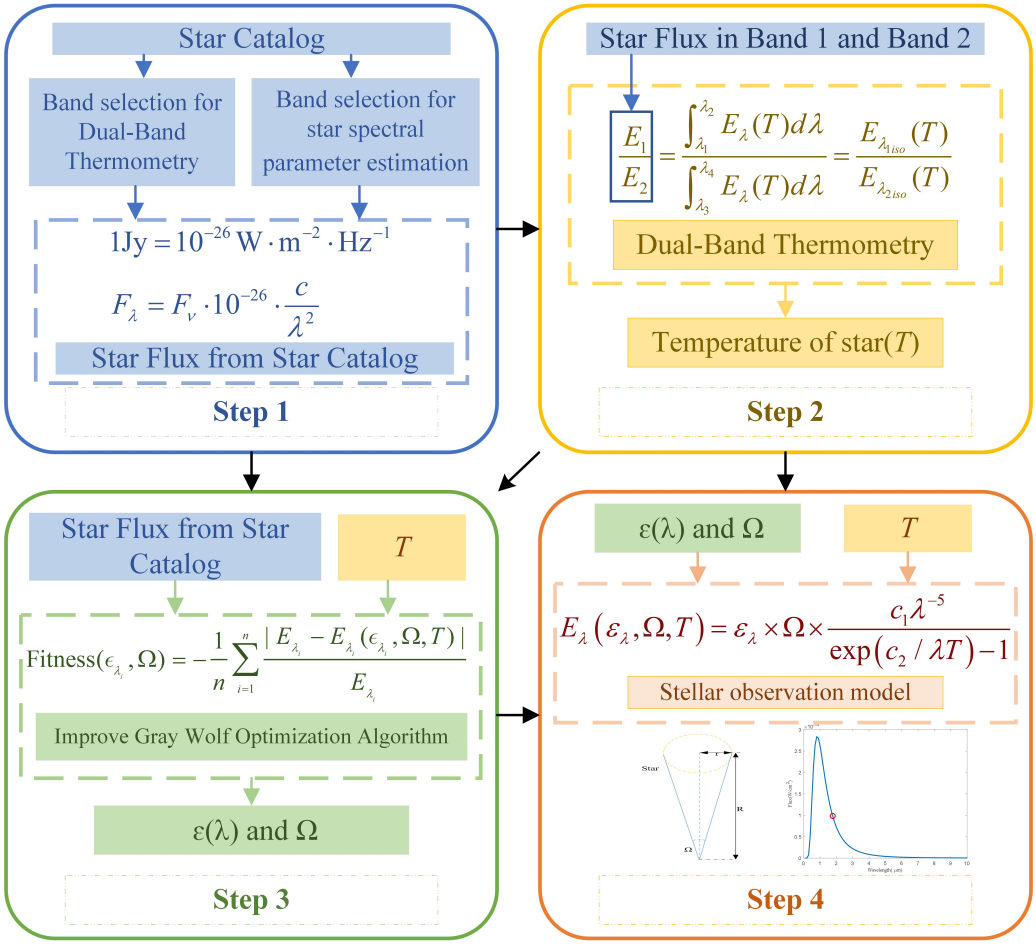

Figure 1. Flowchart of our proposed method.

In order to estimate the radiation flux of a star within a specific target band, it is essential to first determine the star's temperature, emissivity, and observation angle using the known radiation intensity data available in catalogs. These parameters serve as the foundation for accurately estimating the radiation intensity within the target band.

Stellar infrared fluxes are typically expressed in Jansky (Jy) units in stellar catalogs. The Jansky is a quite small unit specifically designed to measure the flux density of celestial objects in astronomical observations. It is generally denoted by F_v, and we can convert F_v into the wavelength-based radiation intensity F_λ:

$$F_\lambda = F_v \times 10^{-26} \times \frac{c}{\lambda^2},\ 1\ \text{Jy} = 10^{-26}\ \text{W}\cdot\text{m}^{-2}\cdot\text{Hz}^{-1} \quad (2)$$

where c is the speed of light and λ is the wavelength. To improve computational efficiency and computational accuracy, we calculated the isophotal radiation fluxes in the catalog based on isophotal wavelengths. The isophotal wavelength is defined as follows [22]:

$$F(\lambda_{iso}) = \frac{\int \lambda F(\lambda) S(\lambda) d\lambda}{\int \lambda S(\lambda) d\lambda} \tag{3}$$

where λ_{iso} is the isophotal wavelength, $S(\lambda)$ is the system's relative spectral response (RSR), and $F(\lambda)$ is the spectral energy distribution of the target (star). Therefore, the radiative information in the catalog can be expressed by the stellar observation model as follows:

$$F_{\lambda_{iso}} = F_v \times 10^{-26} \times \frac{c}{{\lambda_{iso}}^2} = E_{\lambda_{iso}}\left(\varepsilon_{\lambda_{iso}}, \Omega, T\right) \tag{4}$$

Each catalog gives the corresponding isophotal wavelengths, and the isophotal wavelengths corresponding to the MSX catalog bands are shown in Table 1. Table 1 presents the isophotal wavelengths (Isophotal λ) for each band in the MSX catalog, along with the wavelength range, where the radiation intensity reaches 50% of its peak (50% peak intensity) and the corresponding isophotal bandwidth (Isophotal BW).

Table 1. MSX spectral bands.

Band	Isophotal λ (μm)	50% Peak Intensity	Isophotal BW (μm)
A	8.28	6.8–10.8	3.36
B1	4.29	4.22–4.36	0.104
B2	4.35	4.24–4.45	0.179
C	12.13	11.1–13.2	1.72
D	14.65	13.5–15.9	2.23
E	21.34	18.2–25.1	6.24

The primary challenge in estimating stellar spectral parameters lies in the variability of emissivity across different bands, making the problem of parameter estimation similar to solving an underdetermined system of equations. Generally, there are three distinct absorption bands in stellar spectra in the infrared wavelength band, which are the CO overtone absorption band (2.2–3.0 μm), the CO fundamental absorption band (4.0–6.7 μm), and the SiO fundamental absorption band (7.3–11.0 μm) [23]. In response to these spectral features, we divided the MSX catalog bands corresponding to the stellar infrared spectral feature regions into three regions based on the infrared stellar spectral properties: region I for band A (6.8–10.8 μm), region II for band B1 (4.22–4.36 μm) and band B2 (4.24–4.4 μm), and region III for band C (11.1–13.2 μm), band D (13.5–15.9 μm), and band E (18.2–25.1 μm). This is assuming that the stellar emissivity is consistent within each band region. In order to obtain the emissivity in each region, one band in each region needs to be selected as the input.

2.2. Dual-Band Thermometry

The difficulty in estimating stellar spectral parameters from catalog data arises from the imbalance between the number of unknown variables and the limited number of available equations. In order to mitigate this challenge and enhance the accuracy and stability of parameter estimation, we propose utilizing a dual-band thermometry approach to determine stellar temperatures, which can reduce the number of unknown variables. This dual-band thermometry method operates as follows [21]. Assuming that the true

temperature of the space target is T, the infrared irradiance in any two different infrared bands is

$$R(T) = \frac{E_{\lambda_{1iso}}}{E_{\lambda_{2iso}}} = \frac{\varepsilon_{\lambda_{1iso}} \frac{c_1}{{\lambda_{1iso}}^5} \frac{1}{exp\left(\frac{c_2}{\lambda_{1iso} T}\right)-1}}{\varepsilon_{\lambda_{2iso}} \frac{c_1}{{\lambda_{2iso}}^5} \frac{1}{exp\left(\frac{c_2}{\lambda_{2iso} T}\right)-1}} = \frac{{\lambda_{2iso}}^5}{{\lambda_{1iso}}^5} \frac{exp\left(\frac{c_2}{\lambda_{2iso} T}\right)-1}{exp\left(\frac{c_2}{\lambda_{1iso} T}\right)-1} \tag{5}$$

where $E_{\lambda_{1iso}}$ and $E_{\lambda_{2iso}}$ are radiation fluxes in the catalog and $\varepsilon_{\lambda_{1iso}}$ and $\varepsilon_{\lambda_{2iso}}$ are the stellar emissivity at λ_{1iso} and λ_{2iso}, respectively. By assuming that the emissivity remains consistent across both bands, we acknowledge that while the emissivity of stars may vary slightly between different bands, these variations are not significantly disparate. This assumption allows us to simplify the model, thereby facilitating a more streamlined temperature estimation process that still achieves relatively high accuracy. We emphasize that this simplification is made to enhance the practicality of the model without substantially compromising its effectiveness in providing reliable temperature estimates for further stellar radiative flux calculations.

2.3. Improving the Grey Wolf Optimization Algorithm

For the problem of parameter estimation using an optimization algorithm, we establish a corresponding objective function:

$$Fitness\left(\varepsilon_{\lambda_i}, \Omega\right) = \frac{1}{n} \sum_{i=1}^{n} \frac{\left|E_{\lambda_i} - E_{\lambda_i}\left(\varepsilon_{\lambda_i}, \Omega, T\right)\right|}{E_{\lambda_i}} \tag{6}$$

where E_{λ_i} is the radiation flux of a star at λ_i in the star catalog, $E_{\lambda_i}\left(\varepsilon_{\lambda_i}, \Omega, T\right)$ is estimated by the optimization algorithm, and n is the number of selected bands. The goal of this study is to find the optimal band emissivity ε_{λ_i} as well as the stellar observation solid angle Ω by minimizing the fitness function. Considering the nonlinear characteristics of the fitness function, we developed an improved grey wolf optimization (I-GWO) algorithm, which incorporates periodic parameter enhancement for optimal estimation. This method substantially improves the robustness and accuracy of the estimation process, offering significant advantages over traditional approaches.

Grey wolf optimization (GWO) was proposed by Mirjalili et al. in 2014, and it primarily mimics the predation process of grey wolf packs in nature [22]. The algorithm is based on a mathematical model of the social hierarchy of wolves, with stalking, encirclement, and attacking during hunting. Among them, the social hierarchy can be divided into four levels: alpha (α), beta (β), delta (δ), and omega (ω). The hierarchical guidance mechanism prioritizes α, β, and δ as the individuals closest to and second in and second out from the target point, respectively, and the remaining individuals are named ω so that the position update of ω is guided by α, β, and δ to complete the predation process.

The mathematical model of the process of encircling prey is as follows:

$$X(t+1) = X_p(t) - A \times D \tag{7}$$

$$D = \left|C \times X_p(t) - X(t)\right| \tag{8}$$

where t is the number of iterations, X_p is the position of the prey, X is the location of the grey wolves, and A and C are the coefficients of the vector. The following are the calculations of coefficients A and C:

$$A = a \times (2 \times rand_1 - 1),\ a = 2 - t \times \frac{2}{Max_{iter}} \tag{9}$$

$$C = 2 \times rand_2 \tag{10}$$

where a linearly decreases from 2 to 0 as the number of iterations increases, t is the current iteration number, and Max_{iter} is the maximum iteration number, while $Rand_1$ and $rand_2$ are random numbers in the range [0,1].

After obtaining the position model, the next step is to perform a position update of ω for α, β, and δ:

$$D_j = \left|C_i \times X_j(t) - X(t)\right|, i \in 1,2,3\ j \in \alpha,\ \beta,\ \delta \tag{11}$$

$$X(t+1) = \frac{\sum_{i=1}^{3} X_i}{3},\ X_i = X_j(t) - A_i \times D_j \tag{12}$$

Although GWO has outstanding estimation performance, it also still suffers from the problem of falling into a local optimum for some complex problems. The GWO method is analyzed as a global search for potential prey when $A \geq 1$ and a local search when $A < 1$, where A in the GWO method is determined by the parameter a. Therefore, parameter a is the key to balancing the abilities of global search and local exploitation. While the linearly decreasing strategy, as described in the previous, provides a foundational approach to parameter tuning, it is not the most efficient one. Chiu et al. found that the periodic dynamic tuning strategy had better results [24], and thus we introduced a parameter-tuning strategy based on the periodic variation of the cos function:

$$a = 1 + \cos\left(\frac{2\pi t}{Max_{iter}}\right) \tag{13}$$

The two parameters' dynamic tuning strategies are shown in Figure 2.

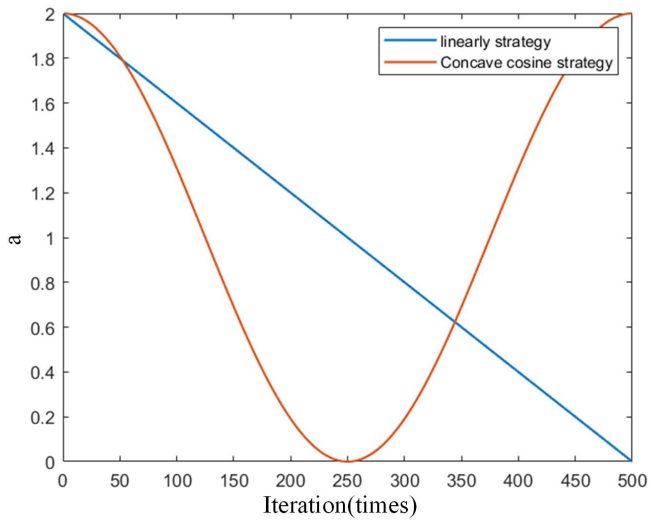

Figure 2. Adjustment of parameters for different strategies.

In our method, the other algorithmic parameters were set as follows. The population size was defined to be 30; the maximum number of iterations was set to 500; and the spatial dimension, which corresponds to the number of variables in the fitness function, was set to 4. Furthermore, the optimization process also involves the expected search range for estimated parameters. The expected range for the observation angle parameter was set to 1.0×10^{-26}–1.0×10^{-10} [20], and the range for the emissivity of bands was set between 0.9 and 1.0 [25]. These ranges determine the search boundaries for the grey wolf population. Algorithm 1 specifically illustrates the process by which the improved grey wolf optimization algorithm searches for the optimal solution.

Algorithm 1 I-GWO: Improved grey wolf optimizer for parameter estimation (ε_λ, Ω)

Input: $fitness(\ \varepsilon_\lambda,\ \Omega)$; number of wolves n = 30; dimensions d = 4; max iterations Max_{Iter} = 500.
Initialization: $X_i = [\ \varepsilon_{\lambda_i}, \Omega_i]$; set iteration counter $t = 1$;
Generate initial wolf pack positions X_i^0 for i = 1 to n, $\varepsilon_{\lambda_i} \in [0.9, 1]$,
$\Omega \in \left[10^{-26}, 10^{-10}\right]$;
Calculate fitness for each wolf ($F(i)$) and identify alpha (X_α), beta (X_β), and delta (X_δ) positions.
while t <= Max_{Iter} **do**
  for each wolf i = 1 to n **do**
    Update the position of the wolf based on X_α, X_β, and X_δ positions.
    Calculate the fitness of the new position ($F(i)$).
  end for
  Update X_α, X_β, and X_δ wolves based on the best fitness values found.
  t=t+1;
end while
Output: Best solution found [ε_λ, Ω] = X_α

3. Experimental Results and Analysis

As can be seen in Section 2, the factors affecting the accuracy of the radiation flux estimation in the target band were mainly the accuracy of the dual-band thermometry and the estimation accuracy of the optimization algorithm. In order to verify the effectiveness and stability of the proposed method for radiation flux estimation, we experimentally analyzed these influencing factors separately. Meanwhile, we also compared the proposed method with other extrapolation methods based on star catalogs to prove the effectiveness of the method. In the experimental section, the best-performing data groups in all tables are highlighted in bold to facilitate quick identification by readers.

3.1. Dual-Band Thermometry Band Selection

In dual-band thermometry, the accuracy of temperature estimation largely depends on the chosen bands. Given the assumption of consistent emissivity, it is crucial to identify band combinations that are affected the least by emissivity variations to determine the most suitable bands for the dual-band thermometry method. Here is the method for calculating the error of temperature estimation:

$$T_{error} = \frac{|T_{cal} - T_{real}|}{T_{real}} \times 100\% \tag{14}$$

where T_{cal} is the calculated stellar temperature and T_{real} is the true stellar temperature.

For the simulation experiment, the emissivity ratio (ε_{ratio}) range was set between 0.95 and 1.05, and the simulated temperature estimation for stars was set in the range from 3000 K to 13,000 K. In the simulation, we assumed that the emissivity of the star was equal in two bands, and we calculated the temperature estimation errors under different temperature and emissivity ratio conditions:

$$\varepsilon_{ratio} = \frac{\varepsilon_{\lambda_1}}{\varepsilon_{\lambda_2}} \tag{15}$$

where ε_{λ_1} is the first band's emissivity and ε_{λ_2} is the second band's emissivity.

Figure 3a–k illustrates the distribution of temperature estimation errors under varying conditions. These charts were derived from simulations where we varied the emissivity ratios and temperatures of the stars. Each subfigure corresponds to a specific wavelength pair used in the dual-wavelength temperature estimation method. In this experiment, we found that when the emissivity ratio was not equal to one, using the dual-wavelength temperature estimation method introduced certain errors. However, selecting different

wavelength pairs could mitigate the impact of emissivity ratio variations on temperature estimation errors. In Figure 3a–d,j–k, it is evident that when the chosen wavelength pairs were closer, variations in the emissivity ratio had a more significant impact on the temperature estimation results. Conversely, in Figure 3e–h, it can be seen that the impact of emissivity ratio variations was relatively smaller.

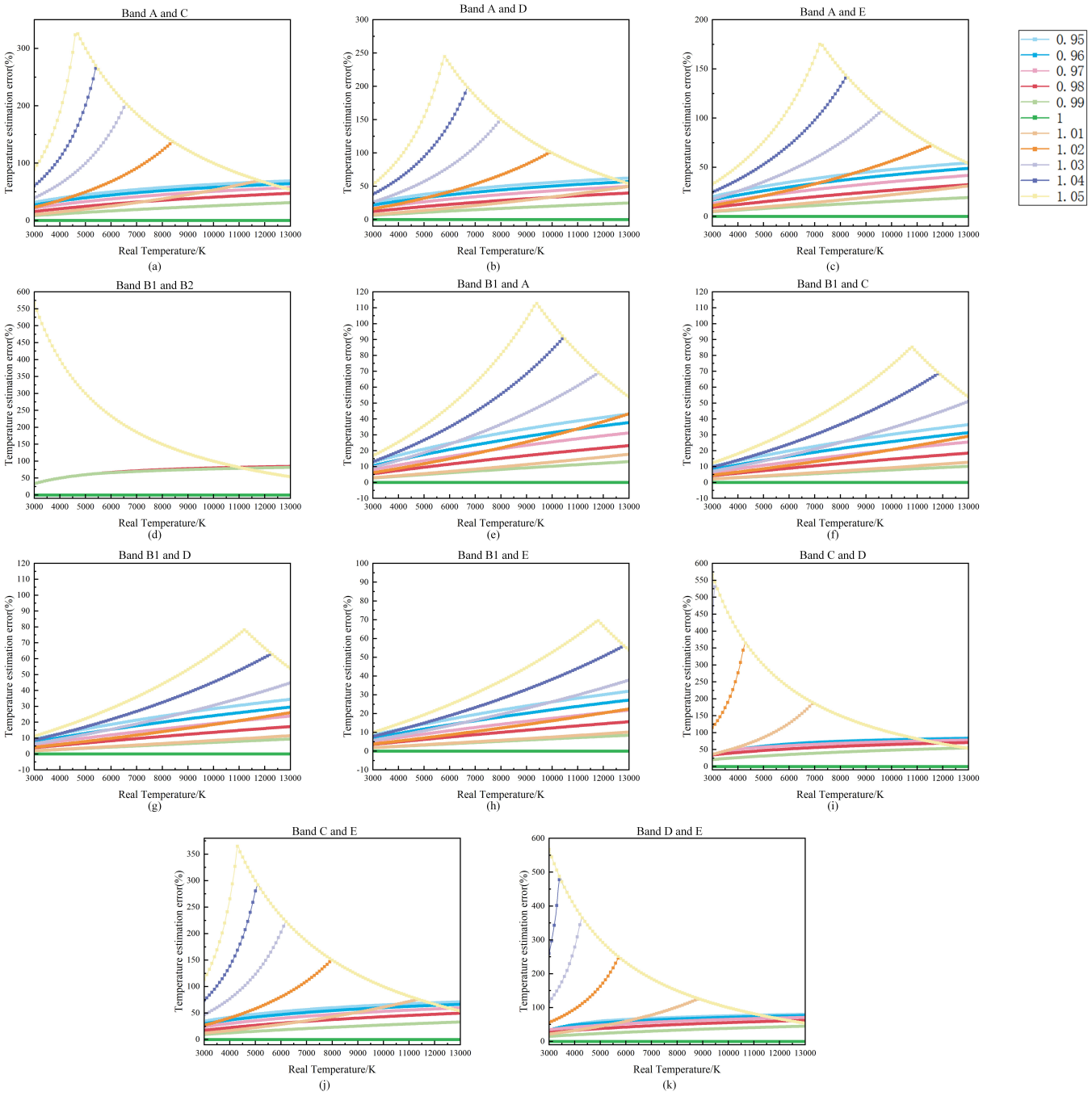

Figure 3. Temperature estimation errors versus emissivity ratios for different temperature stars in different band combinations.

Therefore, selecting bands with certain wavelength differences not only achieved a higher temperature estimation accuracy but also effectively mitigated the influence of emissivity variability on the results, thereby enhancing the accuracy and stability of temperature estimates. The main reason for this result is that the selection of bands with

a wide range of wavelengths captured the radiative properties of the object over a wider range of temperatures, thus providing more information about the temperature.

In addition, it was observed that the error in temperature estimation tended to increase as the temperature itself rose. However, within the infrared band, the predominant calibration stars—comprising K-type, A-type, and G-type stars, as well as cold DA-type white dwarfs—had temperatures below 10,000 K [26]. As a result, the temperature estimation error for these types of stars remained relatively modest, mitigating potential inaccuracies in the calibration processes.

In order to further prove the effectiveness of the dual-band temperature measurement, we selected 351 stars from the MSX catalog with temperatures ranging from 4000 K to 7000 K for temperature estimation. These stars include a range from cooler K-type stars to hotter F-type stars, representing a diverse sample in terms of stellar properties. This selection allows for a comprehensive validation of our temperature estimation methods across different stellar types and conditions. The results of the temperature estimation are shown in Figures 4 and 5. The estimation errors were calculated by comparing our estimated temperatures with the temperatures of the stars investigated in [20]. An analysis of Figure 4 reveals that the combination of band B with other bands, compared with other combinations, achieved the highest estimation accuracy, particularly the combination of B1 with either the C or D bands.

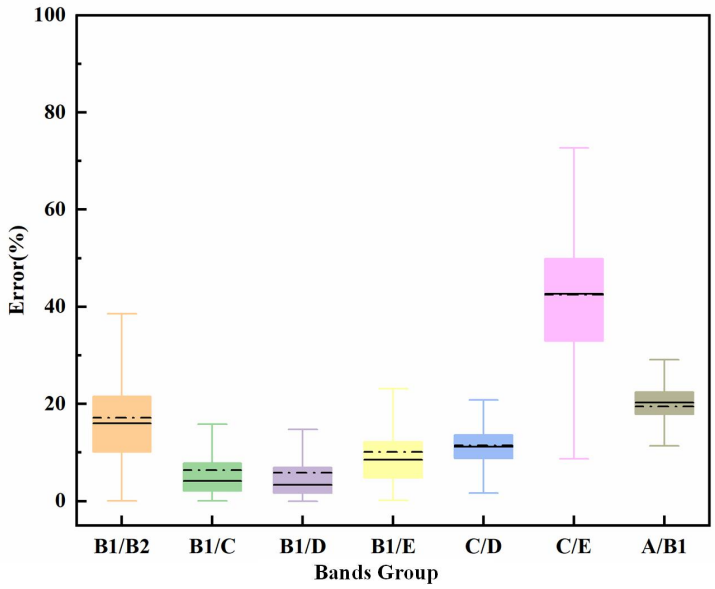

Figure 4. Temperature estimation errors versus different band combinations.

In Figure 5a, the gray area represents an error margin of 10%. It is observable that the majority of the red dots are located within this gray area, outnumbering the blue dots significantly. This indicates that the estimated stellar temperatures using the proposed method predominantly fell within an error margin of less than 10%, demonstrating greater efficacy than the stochastic particle swarm optimization (SPSO) method [20]. Additionally, a statistical analysis of the error results depicted in Figure 5b reveals that 83.5% of the errors were less than 10%, with an average error of 5.82%. The estimation error here, in addition to the error in the dual-band thermometry, also included a systematic error of 3% in the MSX star catalog [27]. Furthermore, compared with the temperature estimation based on the SPSO method, our approach achieved an overall accuracy improvement of 10.8%.

Finally, to demonstrate that the error in temperature estimation does not significantly impact subsequent radiative flux estimates, we conducted further experiments on these 351 stars. We estimated the radiative flux in band E using the fluxes in bands A, B, and C and compared these estimates with the actual fluxes in band E from the MSX star catalog. The results in Figure 5c show an average estimation error of 1.6054%.

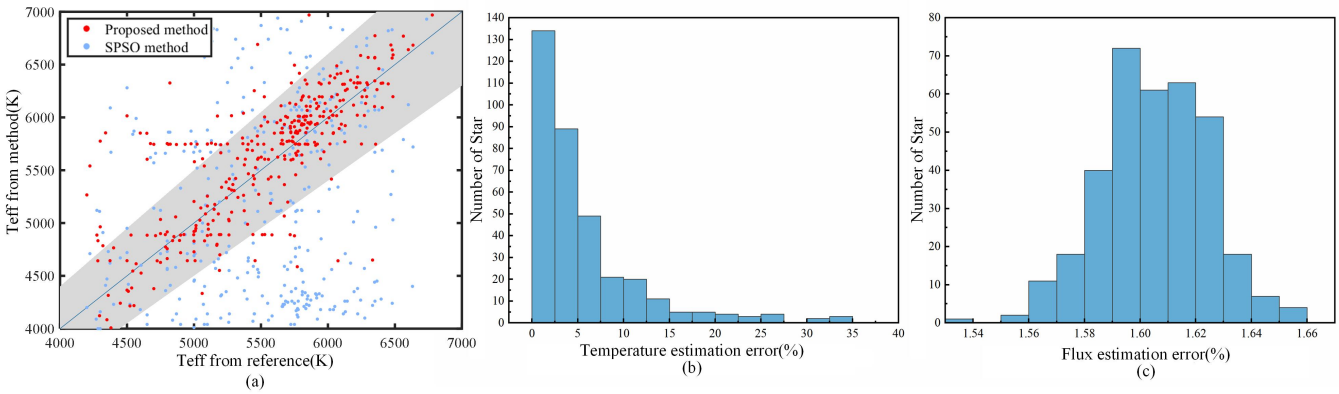

Figure 5. Temperature estimation results for 351 stars from the MSX catalog. (**a**) The Teff from different methods versus the Teff from the reference. (**b**) Histogram of Teff estimation error. (**c**) Histogram of flux estimation error.

3.2. Selection of Optimization Algorithm

In order to evaluate the effectiveness and stability of the I-GWO method in estimating spectral parameters, it was compared with seven advanced and well-known metaheuristic algorithms: particle swarm optimization (PSO) [28,29], the grey wolf optimizer (GWO) [30], the whale optimization algorithm (WOA) [31], dung beetle optimization (DBO) [32], the sine cosine algorithm (SCA) [33], hybrid GWO-PSO [34], and the Coati optimization algorithm (COA) [35]. In this experiment, to ensure uniform experimental conditions, all of the optimization algorithms used operated within the same decision variable boundaries of the target function. Specifically, the emissivity range was set between 0.9 and 1 [36], and the observation angle varied from 1×10^{-26} to 1×10^{-10} [20]. In order to ensure the fairness and comparability of the experiments, the initial population size for all algorithms was uniformly set to 30, and the maximum number of iterations was fixed at 500. Additionally, to minimize the impact of randomness on the experimental outcomes, each algorithm underwent 100 repeated estimations. Subsequently, the average best fitness values and standard deviations (STDs) of these estimations were calculated.

Table 2 details the parameter settings for the various optimization algorithms and displays the results from these 100 experiments. The PSO parameters include the inertia weight (ω), cognitive coefficient (c_1), and social coefficient (c_2); the dung beetle optimization (DBO) algorithm includes the following parameters: rolling dung beetle (RDB), spawning dung beetle (EDB), foraging dung beetle (FDB), and stealing dung beetle (SDB); the convergence parameter (a) in GWO, the WOA, the SCA, and I-GWO balances the local and global components, facilitating both exploration and exploitation; and GWO-PSO involves parameters such as the convergence parameter (a), inertia weight (ω), cognitive coefficient (c_1), and social coefficient (c_2). Additionally, the COA method only required the setting of some common parameters, as mentioned earlier.

As depicted in Figure 6a, while several methods exhibited approximately the same convergence speed for this problem's estimation, the PSO algorithm notably failed to align with this trend. However, the I-GWO method stood out with a lower best fitness value, indicating superior performance. Furthermore, Table 2 demonstrates the stability of the I-GWO method, as evidenced by the minimized standard deviation across 100 calculations. These results reinforce the proposed method's reliability and effectiveness in achieving precise estimations.

Table 2. Parameter settings and 100 experimental results for different optimization algorithms.

Algorithm	Parameter Setting	Mean Best Fitness	STD
PSO	$c_1 = c_2 = 2, \omega = 0.8$	1.39×10^{7}	2.68×10^{7}
SCA	a = 2	1.29×10^{4}	3.28×10^{4}
GWO	$a = 2 \times (1 - \frac{t}{tmax})$	1.90×10^{-4}	7.10×10^{-5}
WOA	$a = 2 \times (1 - \frac{t}{tmax})$, b = 1	1.30×10^{-2}	4.38×10^{-3}
DBO	RDB = 6, EDB = 6, FDB = 7, SDB = 11	7.03×10^{-3}	6.92×10^{-3}
GWO-PSO	$c_1 = c_2 = 2, \omega = 0.8$, $a = 2 \times (1 - \frac{t}{tmax})$	9.91×10^{-4}	3.59×10^{-4}
COA	\	2.49×10^{-2}	2.10×10^{-2}
I-GWO	$a = 1 + \cos(\frac{2\pi t}{Max_{iter}})$	3.23×10^{-6}	2.05×10^{-6}

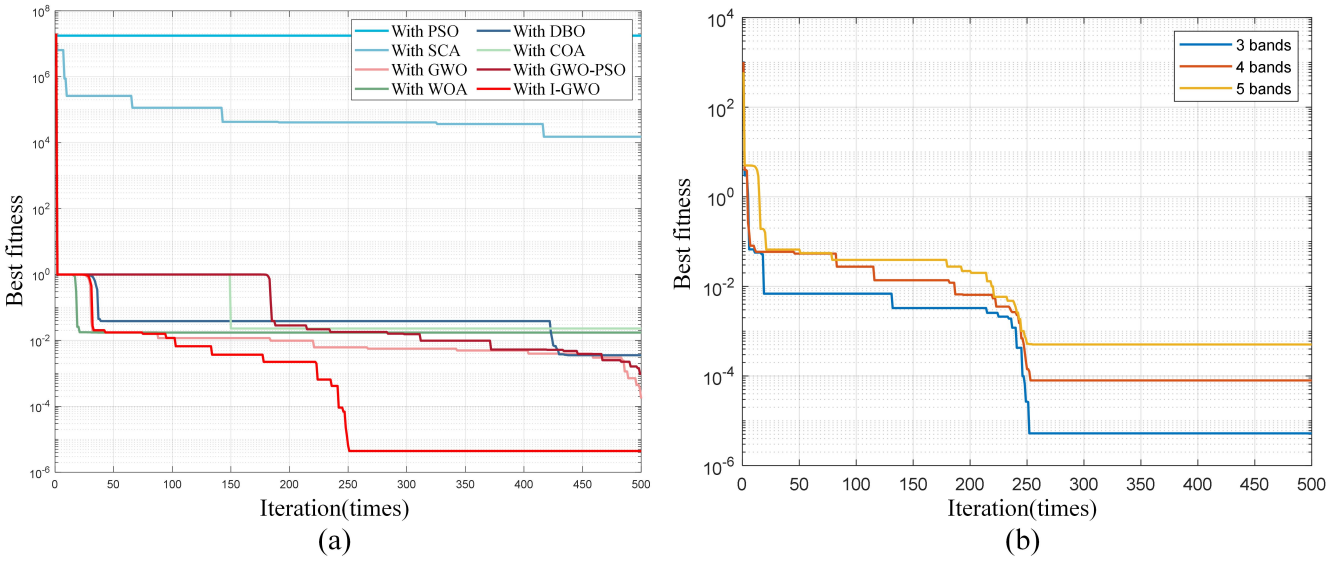

Figure 6. (**a**) Convergence curves with different algorithms. (**b**) Convergence curves with different numbers of bands.

3.3. Selection of Bands Required for Emissivity and Observation Angle Estimation

In addition to selecting a band for effective temperature estimation, it is crucial to choose appropriate bands for estimating other spectral parameters, such as the emissivity ε_{λ_i} and observation angle Ω. In order to investigate a reasonable number of bands and optimize parameter estimation, a comparative analysis of different numbers of band inputs (three, four, and five bands) was carried out in this study. Figure 6b displays the convergence curve of the MSX catalog for estimating the spectral parameters using the inputs of different numbers of bands. It reveals that the smallest value for best fitness was obtained when the inputs used three bands, indicating that a combination of three bands is most effective for parameter estimation.

Furthermore, selecting the appropriate combination of these three bands is crucial. Therefore, we propose the following combination plans, as detailed in Table 3, which are based on the MSX catalogs and the characteristics of the stellar spectral features in the infrared band.

Table 3. Different combination plans.

Group Name	Constituent Bands
Group 1	A, B1, C
Group 2	A, B1, D
Group 3	A, B1, E

The proposed combination plans for estimating spectral parameters, which are predicated on the assumption that the emissivity remains constant within the same infrared spectral feature region, facilitated the construction of stellar infrared spectra. From these spectra, the stellar radiation fluxes across the remaining wavelength bands were computed. These computed fluxes were then compared with the observed values from the catalog to determine the estimation errors. The formula for calculating the radiation flux estimation error is as follows:

$$F_{error} = \frac{|F_{cal} - F_{cat}|}{F_{cat}} \times 100\% \quad (16)$$

where F_{cal} is the calculated stellar radiation flux and F_{cat} is the stellar radiation flux in the catalog.

In order to evaluate the effectiveness of the three mentioned combination plans, we randomly selected 1000 stars from the MSX catalog for analysis. The comparative results of the estimation errors for each combination are presented in Table 4. The accuracy of estimating radiation fluxes for unknown bands was assessed to evaluate the three combination plans. The unknown bands shared by Group 1 and Group 2 were B1 and E. According to the data in Table 4, the estimation accuracy of Group 1 for band E was 1.28%, and that of Group 2 was 1.61%, which shows that the estimation accuracy of Group 1 was better than that of Group 2 as a whole. Meanwhile, the unknown bands common to both Group 1 and Group 3 were B1 and D. Notably, Group 1 achieved an estimation accuracy of 0.288% for band D, which was significantly superior to the accuracy of Group 3 at 1.41%. In addition, when considering the six bands together, Group 1 has the smallest overall estimation error. Based on the above analysis, we identified the combination of bands A, B1, and C as the optimal choice for estimating stellar spectral parameters.

Table 4. Estimation errors of individual bands for different combination plans.

Group Name	A (%)	B1 (%)	B2 (%)	C (%)	D (%)	E (%)	Sum (%)
Group 1	0.00127	0.0521	0.00125	0.00119	0.288	1.28	**1.62**
Group 2	0.00126	0.0579	0.00121	0.265	0.00122	1.61	1.94
Group 3	0.00125	0.0303	0.00115	1.04	1.41	0.00126	2.48

Furthermore, to further validate the effectiveness of our approach, we selected Vega, Sirius, and Arcturus for extrapolative estimation, as these stars have been observed multiple times. The comparative data for Sirius and Vega came from Cohen [16,37], while the comparative data for Arcturus came from SWS [38]. As can be seen in Tables 5 and 6, it is evident that the results derived from our method were in tremendous agreement with the experimental measurements, with a maximum error of 4.589%. This error encompassed not only our estimation inaccuracies but also the systematic discrepancies between the MSX star catalog and the observations by ISO. These results affirm the consistency of our method with empirical data and underscore the reliability of the extrapolation technique.

Table 5. Sirius and Vega flux measurements and errors.

Sirius				Vega			
Wavelength (μm)	**Cohen (F_λ)**	**Ours (F_λ)**	**Error (%)**	**Wavelength (μm)**	**Cohen (F_λ)**	**Ours (F_λ)**	**Error (%)**
2.208	1.392×10^{-13}	1.405×10^{-13}	0.959	2.208	3.940×10^{-14}	3.916×10^{-14}	0.615
2.179	1.463×10^{-13}	1.477×10^{-13}	0.963	2.179	4.139×10^{-14}	4.113×10^{-14}	0.639
3.781	1.806×10^{-14}	1.798×10^{-14}	0.447	3.781	5.162×10^{-15}	5.125×10^{-15}	0.709
3.759	1.843×10^{-14}	1.839×10^{-14}	0.219	3.761	5.263×10^{-15}	5.231×10^{-15}	0.612
4.77	7.350×10^{-15}	7.294×10^{-15}	0.764	4.769	2.107×10^{-15}	2.094×10^{-15}	0.601
8.758	6.776×10^{-16}	6.758×10^{-16}	0.269	8.756	1.955×10^{-16}	1.958×10^{-16}	0.167
10.472	3.332×10^{-16}	3.321×10^{-16}	0.340	10.472	9.631×10^{-17}	9.651×10^{-17}	0.212
11.655	2.178×10^{-16}	2.174×10^{-16}	0.165	11.653	6.308×10^{-17}	6.331×10^{-17}	0.364

Cohen (F_λ) is from Cohen [16,37].

Table 6. Arcturus flux measurements and errors.

Arcturus			
Wavelength (μm)	**SWS (F_λ)**	**Ours (F_λ)**	**Error (%)**
2.4	4.186×10^{-13}	4.378×10^{-13}	4.589
2.6	3.327×10^{-13}	3.307×10^{-13}	0.600
5.612	1.890×10^{-14}	1.933×10^{-14}	2.254
8.268	4.297×10^{-15}	4.379×10^{-15}	1.899
9.354	2.700×10^{-15}	2.737×10^{-15}	1.360
10.57	1.719×10^{-15}	1.702×10^{-15}	1.001
10.91	1.507×10^{-15}	1.504×10^{-15}	0.178
11.6	1.179×10^{-15}	1.184×10^{-15}	0.446

SWS (F_λ) is from ISO [38].

3.4. Comparison of Estimation Methods

In order to prove the validity and stability of the proposed method, the proposed method was compared with two mainstream catalog-based methods: the method based on blackbody estimation (Blackbody Method) [17] and the method considering emissivity (Emissivity Method) [20]. In this experiment, 1000 stars in the MSX catalog were randomly selected as experimental objects, and the A, B1, and C bands were used as inputs to estimate the flux of these stars in band D.

As shown in Figure 7 and Table 7, when compared with other star catalog-based estimation methods, our approach achieved a 75.4% improvement in estimation accuracy and a 91.3% enhancement in estimation stability. This not only attests to the efficacy of our approach across various star types but also highlights its capability to achieve high accuracy. At the same time, the results in the fifth column of Table 7 show that the processing time required by our method constituted merely 3% of the time required by other methods. This result indicates that using the isophotometric flux method is faster than other methods, such as integrating over the whole band, while ensuring the accuracy of the estimation.

Table 7. Estimation results for D band of different methods.

Method	**Time(s)**	**Mean Error (%)**	**STD**
Blackbody Method	2.625	2.3325	1.5537
Emissivity Method	2.582	1.1522	0.1937
Proposed Method	**0.059**	**0.2824**	**0.0169**

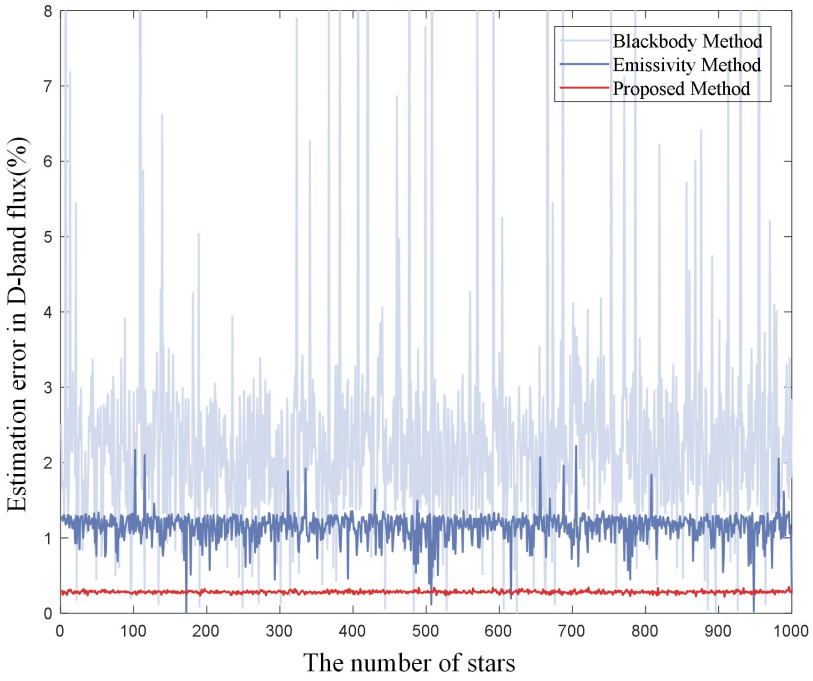

Figure 7. Estimation results for D band of different methods.

3.5. Analysis of Star Calibration Errors

The star calibration process primarily utilizes stars as reference sources to perform absolute radiative calibration across the entire optical path for large-aperture cameras. As illustrated in Figure 8a, stellar radiation enters and passes through the optical system before reaching the detector's imaging system for imaging. Figure 8b depicts the process of star calibration, with the radiative calibration formula expressed as follows:

$$DN_{star} = k \times L_{star} + b \tag{17}$$

where DN_{star} represents the digital number value of the star in the image, L_{star} is the calibrated star's radiative flux, k is the calibration gain coefficient, and b is the calibration offset coefficient. Therefore, the calibration error in star calibration encompasses not only the uncertainties in the absolute flux of the reference source stars but also includes the errors in the extraction of star energy and the transmission error of standard luminance.

The estimation error for star radiative flux using the star catalogs proposed in this study primarily consisted of the systematic errors of the MSX star catalog σ_c (3%) [27] and the estimation model error σ_s (<1%). The star extraction error σ_e mainly arises from non-uniformities in the pixel response due to the camera manufacturing process. If a star is imaged in different positions on the camera, then this can lead to inconsistencies in the output, approximately ranging from 3% to 5%. The uncertainty σ_t in the transfer of standard luminance is due to the influence of stray light, spot uniformity, and other factors during the radiative transfer process, generally amounting to 1.5%. The accuracy of absolute stellar radiative calibration can be calculated using the root mean square of the sum of the squares of the aforementioned uncertainties, as per Equation (18), which theoretically achieves an accuracy within 6.1%:

$$\sigma_{total} = \sqrt{{\sigma_c}^2 + {\sigma_s}^2 + {\sigma_e}^2 + {\sigma_t}^2} \tag{18}$$

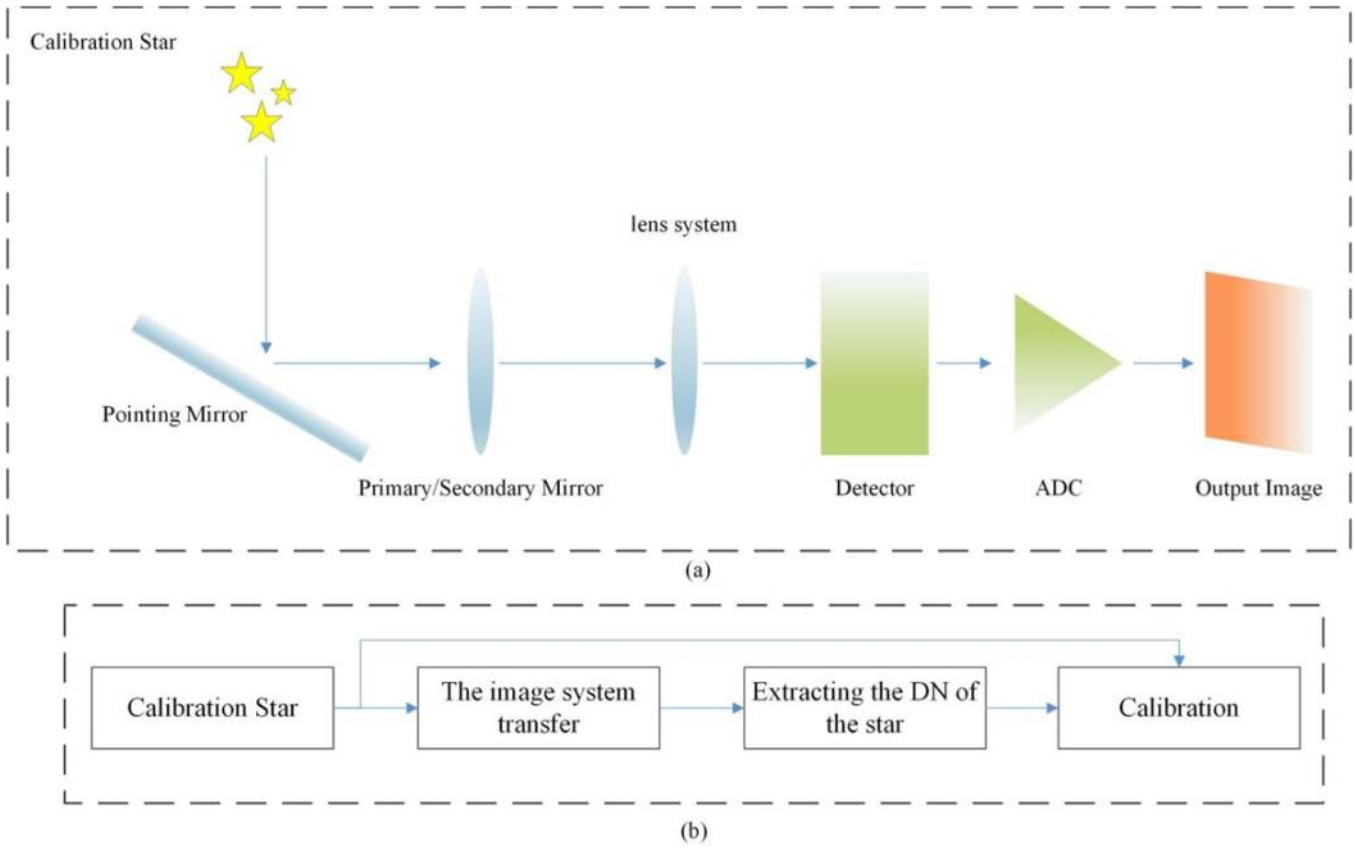

Figure 8. (**a**) Star radiative transfer processes. (**b**) The flow of star calibration.

In order to further validate the effectiveness of the proposed method in practical applications, this study conducted calibration experiments on five selected stars (as indicated in Table 8) using an on-orbit camera, where these stars demonstrated an extrapolation accuracy of less than 1% within the camera's spectral band (8–12 μm). Figure 9 illustrates the calibration outcomes, where the vertical axis represents the camera's digital number (DN) response and the horizontal axis denotes the stellar radiative flux (E). It was observed that the calibration curve achieved a fitting accuracy (R^2) of 0.9995, demonstrating a high level of precision.

Table 8. Catalog of calibration stars (W/cm^2).

Right Ascension (RA)	Declination (DE)	E (W/cm^2)
9.19	44.49	2.137×10^{-16}
316.78	−25.01	3.902×10^{-16}
59.51	−13.51	1.501×10^{-15}
269.15	51.49	2.131×10^{-15}
345.94	28.08	5.270×10^{-15}

Moreover, using the derived calibration curve to estimate the radiative flux of two additional stars with known flux values revealed that the calibration error was less than 5% (Table 9). These experimental outcomes not only prove the effectiveness of the stellar calibration method but also highlight its significance in enhancing the accuracy of stellar radiative flux estimation.

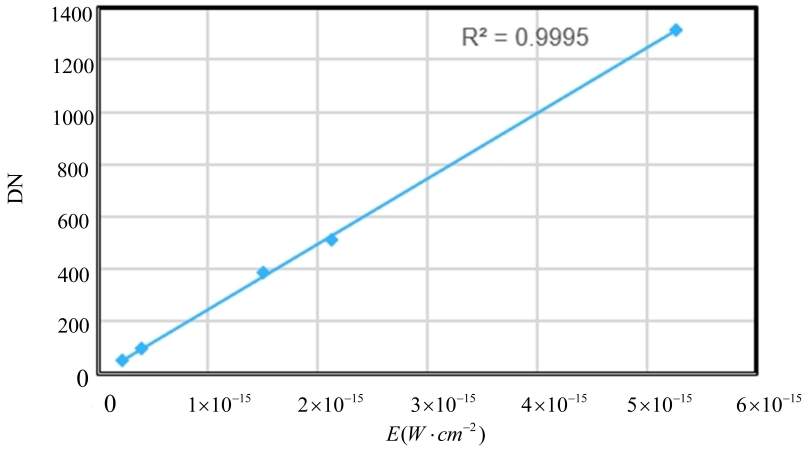

Figure 9. Stellar calibration curve.

Table 9. Inversion results of stellar calibration.

RA	DE	E_{real} (W/cm^2)	E_{inv} (W/cm^2)	Error (%)
258.76	36.81	6.648×10^{-16}	6.87×10^{-16}	3.3
10.13	56.54	8.894×10^{-16}	9.31×10^{-16}	4.7

4. Discussion

This study introduced a novel method for estimating stellar radiative flux based on infrared star catalogs, demonstrating (through experimental validation) significant improvements in estimation accuracy, stability, and computational efficiency over existing star catalog-based techniques. Specifically, when compared with other star catalog-based estimation methods, our approach achieved a 75.4% improvement in estimation accuracy and a 91.3% enhancement in estimation stability, and the computation time was reduced to merely 3% of that required by alternative methods. These advancements were primarily attributed to the introduction of dual-band thermometry and enhancements to the grey wolf optimization algorithm. Concurrently, the application of our method to estimating the radiative flux of three well-known calibration stars (Sirius, Vega, and Arcturus) yielded a radiative flux error less than 5%, thus also providing evidence of our method's efficacy. Furthermore, error analysis revealed that the calibration accuracy of the star radiative fluxes, as established by the proposed method, was within 6.1%. Additionally, the results from the on-orbit experiments demonstrate that the star calibration error remained below 5%.

The dual-band thermometry effectively reduced the number of parameters which needed to be estimated, thereby increasing the overall accuracy of the estimates. Additionally, by analyzing the characteristics of the optimization objective function and incorporating parameters that varied periodically, we refined the grey wolf optimization algorithm by using a periodic variation parameter to more precisely locate optimal solutions, avoiding local minimums and further enhancing the accuracy and stability of parameter estimation. Moreover, by adopting the concept of an isophotal wavelength in place of traditional integration methods, we significantly increased the computational efficiency without sacrificing accuracy.

Despite the progress achieved, there remains room for improvement in the accuracy of radiative flux estimates across specific spectral bands. As indicated by the extrapolation results in Table 6, the error in some bands was still nearly 5%, mainly due to the assumption of uniform emissivity within certain spectral regions, as well as systematic errors from the star catalogs. On one hand, using higher-precision star catalogs for estimates could be beneficial. On the other hand, higher-resolution stellar emissivity as a function of the wavelength needs to be established to improve estimation accuracy further. For example,

the stellar emissivity at a higher wavelength resolution can be estimated by selecting the spectral data provided by the JWST as input data [39–41].

For on-orbit radiometric calibration, despite individual stars having data biases, using the radiative data of a large sample of stars and performing statistical averaging can significantly enhance the overall calibration accuracy.

In summary, the method proposed in this study for estimating the stellar infrared radiation flux using infrared star catalogs demonstrated superior performance in terms of accuracy, stability, and computational efficiency, providing an effective tool for stellar calibration research. However, further investigation into the variability of stellar emissivity across different spectral bands will be a focal point of future work.

5. Conclusions

We investigated the spectral characteristics of stars and a camera observation model and then proposed a method to estimate the infrared radiation flux of stars based on existing infrared star catalog data. The proposed method introduces dual-band thermometry with I-GWO algorithms for estimating the stellar parameters which, when combined with observational models, can achieve the estimation of stellar radiative fluxes in any infrared spectral band. The temperature estimation experiments, which were conducted using MSX catalog observational data, demonstrated that the proposed method achieved an accuracy better than 10% for 83.5% of the stellar temperature estimates within the 4000–7000 K range, with an average error of 5.82%. In addition, the proposed method significantly enhanced the accuracy of radiative flux estimates based on stellar catalog methods. When compared with previous catalog-based methods, our approach achieved a 75.4% improvement in estimation accuracy, with the algorithm's stability improving by 91.3%. The validation of our method's effectiveness was confirmed through comparative analyses with well-known calibration star data, which revealed that our estimation errors remained below 5%. Additionally, the incorporation of isophotal radiation significantly increased the computational efficiency by 96.9%. Through employing the approach outlined in this study, a multitude of benchmark sources with precision exceeding 1% can be provided for stellar calibration, offering a broader array of options for the in-orbit calibration of space cameras. The proposed method offers new possibilities for star calibration. The experimental results indicate that using this method for on-orbit star calibration can achieve a star calibration error within 5%. Furthermore, this method is capable of not only estimating the emissivity of stars within catalog bands but also calculating the effective temperatures of stars, presenting a novel pathway for the exploration of infrared stellar characteristics. Therefore, this approach holds value in remote sensing applications and scientific research.

Author Contributions: Conceptualization, P.R.; methodology Y.H.; software, Y.H. and Y.Z.; validation, Y.H. and Y.Z.; formal analysis, Y.H.; investigation, Y.H. and X.C.; resources, Y.H. and Y.Z.; data curation, Y.H.; writing—original draft preparation, Y.H.; writing—review and editing, Y.Z.; supervision, P.R.; project administration, Y.Z. and X.C.; funding acquisition, P.R. All authors have read and agreed to the published version of the manuscript. All authors reviewed the manuscript.

Funding: This research was funded by National Natural Science Foundation of China (Grant No. 62175251).

Data Availability Statement: The original contributions presented in the study are included in the article, further inquiries can be directed to the corresponding authors.

Conflicts of Interest: The authors declare no conflicts of interest.

References

1. Li, S.; Li, C.; Yang, X.; Zhang, K.; Yin, J. Infrared dim target detection method inspired by human vision system. *Optik* **2020**, *206*, 164167. [CrossRef]
2. Guo, Q.; Chen, F.; Li, X.; Chen, B.; Wang, X.; Chen, G.; Wei, C. High-accuracy source-independent radiometric calibration with low complexity for infrared photonic sensors. *Light Sci. Appl.* **2021**, *10*, 163. [CrossRef] [PubMed]
3. Price, S.D. Infrared irradiance calibration. *Space Sci. Rev.* **2004**, *113*, 409–456. [CrossRef]

4. Mill, J.D.; Guilmain, B.D. The MSX mission objectives. *Johns Hopkins APL Tech. Dig.* **1996**, *17*, 4–10.
5. Cohen, M.; Walker, R.G.; Jayaraman, S.; Barker, E.; Price, S.D. Spectral irradiance calibration in the infrared. XII. Radiometric measurements from the midcourse space experiment. *Astron. J.* **2001**, *121*, 1180. [CrossRef]
6. Egan, M.; Price, S.; Kraemer, K. The Midcourse Space Experiment Point Source Catalog Version 2.3. In Proceedings of the American Astronomical Society, Seattle, WA, USA, 4–7 May 2003; Volume 203, p. 57-08.
7. Reach, W.T.; Megeath, S.; Cohen, M.; Hora, J.; Carey, S.; Surace, J.; Willner, S.; Barmby, P.; Wilson, G.; Glaccum, W.; et al. Absolute calibration of the infrared array camera on the spitzer space telescope. *Publ. Astron. Soc. Pac.* **2005**, *117*, 978. [CrossRef]
8. Krick, J.E.; Lowrance, P.; Carey, S.; Laine, S.; Grillmair, C.; Van Dyk, S.D.; Glaccum, W.J.; Ingalls, J.G.; Rieke, G.; Hora, J.L.; et al. Spitzer IRAC photometry of JWST calibration stars. *Astron. J.* **2021**, *161*, 177. [CrossRef]
9. Xu, X.j.; Li, Z. A Chandra Study of the Stellar X-ray Emissivity of Globular Clusters in the M31 Bulge. *Astrophys. J.* **2018**, *856*, 77. [CrossRef]
10. Basu, R.; Mitra, D.; Melikidze, G.I. Meterwavelength Single-pulse Polarimetric Emission Survey. V. Flux Density, Component Spectral Variation, and Emission States. *Astrophys. J.* **2021**, *917*, 48. [CrossRef]
11. Katz, D.; Soubiran, C.; Cayrel, R.; Adda, M.; Cautain, R. On-line determination of stellar atmospheric parameters Teff, log g,[Fe/H] from ELODIE echelle spectra. I—The method. *arXiv* **1998**, arXiv:astro-ph/9806232 .
12. Castelli, F.; Kurucz, R.L. New grids of ATLAS9 model atmospheres. *arXiv* **2004**, arXiv:astro-ph/0405087.
13. Rieke, G.; Blaylock, M.; Decin, L.; Engelbracht, C.; Ogle, P.; Avrett, E.; Carpenter, J.; Cutri, R.; Armus, L.; Gordon, K.; et al. Absolute physical calibration in the infrared. *Astron. J.* **2008**, *135*, 2245. [CrossRef]
14. Rieke, G.; Lebofsky, M.; Low, F. An absolute photometric system at 10 and 20 microns. *Astron. J.* **1985**, *90*, 900–906. [CrossRef]
15. Rebassa-Mansergas, A.; Gänsicke, B.; Schreiber, M.R.; Koester, D.; Rodríguez-Gil, P. Post-common envelope binaries from SDSS—VII. A catalogue of white dwarf-main sequence binaries. *Mon. Not. R. Astron. Soc.* **2010**, *402*, 620–640. [CrossRef]
16. Wang, Y.-D.; Sun, X.-J.; Zhang, H.; Chen, F.-S. A new approach for extrapolating star flux using cross-matching multiple catalogues. *J. Infrared Millim. Waves* **2019**, *38*, 473–478. [CrossRef]
17. Zhang, C.X.; Yuan, Y.; Zhang, H.W.; Shuai, Y.; Tan, H.P. Estimating stellar effective temperatures and detected angular parameters using stochastic particle swarm optimization. *Res. Astron. Astrophys.* **2016**, *16*, 008. [CrossRef]
18. Suzuki, N.; Fukugita, M. Blackbody stars. *Astron. J.* **2018**, *156*, 219. [CrossRef]
19. Rrapaj, E.; Sieverding, A.; Qian, Y.Z. Rate of dark photon emission from electron positron annihilation in massive stars. *Phys. Rev. D* **2019**, *100*, 023009. [CrossRef]
20. Zhang, C.; Li, T.; Jin, P.; Yuan, Y.; Ouyang, X.; Marchesoni, F.; Huang, J. Extracting stellar emissivity via a machine learning analysis of MSX and LAMOST catalog data. *Phys. Rev. D* **2022**, *106*, 123035. [CrossRef]
21. Di Carolo, F.; Savino, L.; Palumbo, D.; Del Vecchio, A.; Galietti, U.; De Cesare, M. Standard thermography vs free emissivity dual color novel CIRA physics technique in the near-mid IR ranges: Studies for different emissivity class materials from low to high temperatures typical of aerospace re-entry. *Int. J. Therm. Sci.* **2020**, *147*, 106123. . [CrossRef]
22. Mirjalili, S.; Mirjalili, S.M.; Lewis, A. Grey wolf optimizer. *Adv. Eng. Softw.* **2014**, *69*, 46–61. [CrossRef]
23. Engelke, C.W.; Price, S.D.; Kraemer, K.E. Spectral irradiance calibration in the infrared. XVI. Improved accuracy in the infrared spectra of the secondary and tertiary standard calibration stars. *Astron. J.* **2006**, *132*, 1445. [CrossRef]
24. Chiu, C.Y.; Shih, P.C.; Li, X. A dynamic adjusting novel global harmony search for continuous optimization problems. *Symmetry* **2018**, *10*, 337. [CrossRef]
25. Boissier, S.; Prantzos, N.; Boselli, A.; Gavazzi, G. The star formation rate in disc galaxies: Thresholds and dependence on gas amount. *Mon. Not. R. Astron. Soc.* **2003**, *346*, 1215–1230. [CrossRef]
26. Decin, L.; Eriksson, K. Theoretical model atmosphere spectra used for the calibration of infrared instruments. *Astron. Astrophys.* **2007**, *472*, 1041–1053. [CrossRef]
27. Price, S.; Paxson, C.; Engelke, E.; Murdock, T.; Kraemer, K. Air Force Research Lab Hanscom Afb Ma Space Vehicles Directorate. *Absolute Infrared Calibration of Standard Stars by the Midcourse Space Experiment*; Air Force Research Laboratory: Chestnut Hill, MA, USA, 2004.
28. Chiu, C.-Y.; Shih, P.-C.; Li, X. Hybrid algorithm of particle swarm optimization and grey wolf optimizer for improving convergence performance. *J. Appl. Math.* **2017**, *10*, 337. [CrossRef]
29. Qawqzeh, Y.; Alharbi, M.T.; Jaradat, A.; Sattar, K.N.A. A review of swarm intelligence algorithms deployment for scheduling and optimization in cloud computing environments. *PeerJ Comput. Sci.* **2021**, *7*, e696. [CrossRef]
30. Alyu, A.B.; Salau, A.O.; Khan, B.; Eneh, J.N. Hybrid GWO-PSO based optimal placement and sizing of multiple PV-DG units for power loss reduction and voltage profile improvement. *Sci. Rep.* **2023**, *13*, 6903. [CrossRef] [PubMed]
31. Mirjalili, S.; Lewis, A. The whale optimization algorithm. *Adv. Eng. Softw.* **2016**, *95*, 51–67. [CrossRef]
32. Zhu, F.; Li, G.; Tang, H.; Li, Y.; Lv, X.; Wang, X. Dung beetle optimization algorithm based on quantum computing and multi-strategy fusion for solving engineering problems. *Expert Syst. Appl.* **2024**, *236*, 121219. [CrossRef]
33. Mirjalili, S. SCA: A sine cosine algorithm for solving optimization problems. *Knowl.-Based Syst.* **2016**, *96*, 120–133. [CrossRef]
34. Shaheen, M.A.; Hasanien, H.M.; Alkuhayli, A. A novel hybrid GWO-PSO optimization technique for optimal reactive power dispatch problem solution. *Ain Shams Eng. J.* **2021**, *12*, 621–630. [CrossRef]
35. Dehghani, M.; Montazeri, Z.; Trojovská, E.; Trojovskỳ, P. Coati Optimization Algorithm: A new bio-inspired metaheuristic algorithm for solving optimization problems. *Knowl.-Based Syst.* **2023**, *259*, 110011. [CrossRef]

36. Serenelli, A.; Rohrmann, R.D.; Fukugita, M. Nature of blackbody stars. *Astron. Astrophys.* **2019**, *623*, A177. [CrossRef]
37. Cohen, M.; Walker, R.G.; Barlow, M.J.; Deacon, J.R. Spectral irradiance calibration in the infrared. 1. Ground-based and iras broad-band calibrations. *Astron. J.* **1992**, *104*, 1650–1657. [CrossRef]
38. Infrared Processing and Analysis Center (IPAC), California Institute of Technology. Short Wavelength Spectrometer (SWS) Data Archive. Available online: https://irsa.ipac.caltech.edu/data/SWS/index.html (accessed on 1 April 2024).
39. Wright, G.S.; Rieke, G.H.; Glasse, A.; Ressler, M.; Marín, M.G.; Aguilar, J.; Alberts, S.; Álvarez-Márquez, J.; Argyriou, I.; Banks, K.; et al. The mid-infrared instrument for JWST and its in-flight performance. *Publ. Astron. Soc. Pac.* **2023**, *135*, 048003. [CrossRef]
40. Gasman, D.; Argyriou, I.; Sloan, G.; Aringer, B.; Álvarez-Márquez, J.; Fox, O.; Glasse, A.; Glauser, A.; Jones, O.C.; Justtanont, K.; et al. JWST MIRI/MRS in-flight absolute flux calibration and tailored fringe correction for unresolved sources. *Astron. Astrophys.* **2023**, *673*, A102. [CrossRef]
41. JWST Documentation Team. JWST Mid Infrared Instrument. Available online: https://jwst-docs.stsci.edu/jwst-mid-infrared-instrument#gsc.tab=0 (accessed on 8 June 2024).